CRACD loss promotes small cell lung cancer tumorigenesis via EZH2-mediated immune evasion

Shengzhe Zhang,[1,†] Kee-Beom Kim,[2,3†] Yuanjian Huang,[1†] Dong-Wook Kim,[2] Bongjun Kim,[1] Kyung-Pil Ko,[1] Gengyi Zou,[1] Jie Zhang,[1] Sohee Jun,[1] Nicole A. Kirk,[2] Ye Eun Hwang,[2] Young Ho Ban,[4] Joseph M. Chan,[5] Charles M. Rudin,[5] Kwon-Sik Park,[2,‡] Jae-Il Park[1,6,7,‡]

[1]Department of Experimental Radiation Oncology, Division of Radiation Oncology, The University of Texas MD Anderson Cancer Center, Houston, TX 77030, USA
[2]Department of Microbiology, Immunology, and Cancer Biology, University of Virginia School of Medicine, Charlottesville, VA 22908, USA
[3]BK21 FOUR KNU Creative BioResearch Group, School of Life Sciences, Kyungpook National University, Daegu, 41566, Republic of Korea
[4]Hamatovascular Biology Center, Robert M. Berne Cardiovascular Research Center, University of Virginia School of Medicine, Charlottesville, VA 22908, USA
[5]Department of Medicine, Thoracic Oncology Service, Memorial Sloan Kettering Cancer Center, New York, NY 10065, USA
[6]Graduate School of Biomedical Sciences, The University of Texas MD Anderson Cancer Center, Houston, TX 77030, USA
[7]Program in Genetics and Epigenetics, The University of Texas MD Anderson Cancer Center, Houston, TX 77030, USA

[†]These authors contributed equally.
[‡]Correspondence: Kwon-Sik Park (kp5an@virginia.edu) and Jae-Il Park (jaeil@mdanderson.org)
Tel: +1 713-792-3659; Fax: +1 713-794-5369

Keywords: CRACD, CRAD, KIAA1211, small cell lung cancer, immune evasion, EZH2, PRC2, immunotherapy

Competing Interest Statement: The authors declare that they have no conflict of competing interests.

Abstract

The mechanisms underlying immune evasion and immunotherapy resistance in small cell lung cancer (SCLC) remain unclear. Herein, we investigate the role of CRACD tumor suppressor in SCLC. We found that CRACD is frequently inactivated in SCLC, and *Cracd* knockout (KO) significantly accelerates SCLC development driven by loss of *Rb1*, *Trp53*, and *Rbl2*. Notably, the Cracd-deficient SCLC tumors display CD8+ T cell depletion and suppression of antigen presentation pathway. Mechanistically, CRACD loss silences the MHC-I pathway through EZH2. EZH2 blockade is sufficient to restore the MHC-I pathway and inhibit CRACD loss-associated SCLC tumorigenesis. Unsupervised single-cell transcriptomic analysis identifies SCLC patient tumors with concomitant inactivation of CRACD, impairment of tumor antigen presentation, and downregulation of EZH2 target genes. Our findings define CRACD loss as a new molecular signature associated with immune evasion of SCLC cells and proposed EZH2 blockade as a viable option for CRACD-negative SCLC treatment.

Introduction

SCLC accounts for 13% of all lung cancers, and remains a particularly lethal disease, with a 5-year survival rate of 7%. It is estimated to cause approximately 30,000 patient deaths annually in the United States (1, 2). Major contributing factors to the high mortality rate of SCLC patients include the high prevalence of metastasis at the time of diagnosis, which limits therapeutic options, and nearly universal disease relapse associated with resistance to further therapies (3, 4). Notably, immune checkpoint blockade (ICB) approaches designed to target tumors expressing neoantigens are effective in only ~13% of patients with SCLC—a small subset, given that the high mutation burden of SCLC tumors should be sufficient to trigger a robust immune response from cytotoxic T lymphocytes (5-7).

While it remains unclear what underlies the refractoriness of SCLC to ICB and how to stratify patient tumors by the degree of response to ICB, recent studies have explored emerging molecular subtypes of SCLC tumors, classified based on the actions of key lineage transcription factors (ASCL1, NEUROD1, and POU2F3) and inflammation (8-11). However, the current classification system has not been robust enough to reliably predict immunotherapy response. Therefore, understanding how SCLC cells evade immune surveillance and become resistant to immunotherapy is imperative to improve the durability of ICB in responding patients, and to inform strategies to increase the fraction of patients benefitting from ICB.

We recently discovered a tumor suppressor gene called *CRACD* (Capping protein inhibiting regulator of actin dynamics, *CRAD/KIAA1211*) (12). CRACD is ubiquitously expressed in epithelial cells and binds to and inhibits capping proteins (CAPZA and CAPZB), which are negative regulators of actin polymerization (12). CRACD promotes actin polymerization, which is crucial for maintaining the cadherin-catenin-actin complex of epithelial cells. *CRACD* is recurrently mutated or transcriptionally downregulated in cancer cells, which results in reduction of

filamentous actin (F-actin) and disruption of the cadherin-catenin-actin complex (12). These alterations cause loss of epithelial cell integrity and decrease the cytoplasm-to-nucleus volume ratio; cells become “small”. A pathological consequence of these alterations is evident in the intestine, where CRACD inactivation hyperactivates WNT signaling via β-catenin release from the cadherin-catenin-actin complex and accelerates intestinal tumorigenesis (12).

CRACD is also frequently inactivated in SCLC, which led us to hypothesize that CRACD is a tumor suppressor restricting SCLC tumorigenesis. To test the hypothesis, we interrogated the impact of CRACD loss on SCLC development using preneoplastic cells and genetically engineered mouse models (GEMMs) and through immune cell profiling and single-cell transcriptomic analysis of human SCLC tumors. Our findings nominate CRACD as a new tumor suppressor of SCLC and implicate CRACD loss as a new molecular signature relevant to SCLC immune evasion.

Results

CRACD inactivation in the SCLC subtype

CRACD is mutated in 11-16% of SCLC patient tumors and SCLC cell lines, ranking in frequency after *RB1* and *TP53* but more frequently than *RBL2*, *CREBBP,* and *EP300* among validated tumor suppressor genes (Fig. 1A-C, fig. S1)(12-16). CRACD expression was also lower in SCLC tumors than in healthy lung tissue samples (Fig. 1D).

We also examined scRNA-seq datasets of 19 SCLC patient tumor samples and 8 normal human lung samples from previous studies (10, 17) (Fig. 1E, Table S1, S2). A pair-wise correlation analysis showed that SCLC tumor datasets could be divided into two major groups (SC1- and SC2-types) (Fig. 1F). The SC1-type SCLC tumors were clinically associated with recurrence (2 of 3) and metastasis (1 of 3), whereas the SC2-type tumors were mainly associated with primary tumors (6 of 16) and metastases (7 of 16) (Fig. 1G). A copy number variation analysis showed higher genomic instability in the SC2-type than in the SC1-type tumors (Fig. 1H, I). According to the ANPY classification (9), the SC1-type was mainly categorized as ASCL1-type (Fig. 1J). Intriguingly, *CRACD* expression was notably downregulated in the SC1-type compared to the SC2 (Fig. 1K). These results suggest that CRACD inactivation occurs in a specific subtype of SCLC patient tumor cells.

CRACD inactivation accelerates SCLC tumorigenesis

Having observed the CRACD inactivation in SCLC, we hypothesized that CRACD loss-of-function plays a role in SCLC tumorigenesis. To test this hypothesis, we first determined whether *Cracd* knockout (KO) promotes the transformation of preneoplastic precursor cells of SCLC (preSCs). The preSCs were derived from early-stage neuroendocrine (NE) lesions developed in an *Rb1*/*Trp53*-mutant mouse model of

SCLC and upon an oncogenic event, such as *L-Myc* amplification or *Crebbp/Ep300* loss progress to an invasive and fully malignant tumor (13, 18, 19). Utilizing the CRISPR/Cas9-mediated gene editing strategy to generate *Cracd* KO mice as previously described (12), we targeted exon 2 of *Cracd* in preSCs (fig. S2). *Cracd* KO preSCs readily transformed into aggregates and spheres that are typical of SCLC cells in culture and formed subcutaneous tumors in an allograft model significantly faster than did control preSCs (Fig. 2A-E). We also utilized a GEMM in which *Rb1*$^{fl/fl}$, *Trp53*$^{fl/fl}$, and *Rbl2*$^{fl/fl}$ alleles (RPR2) were conditionally deleted on the background of *Cracd* wild-type (WT) alleles or germline *Cracd* KO (*Cracd*, *Rb1*, *Trp53*, and *Rbl2* quadruple KO [CRPR2]) (20, 21). CRPR2 mice showed marked increases in tumor burden and number and mitotic index of SCLC tumors compared to those of RPR2 mice (Fig. 2F-K), indicating that *Cracd* KO accelerates SCLC tumor development *in vivo*. These results strongly suggest that CRACD plays a tumor suppressor role in SCLC development.

Cracd KO increases tumor cell phenotypic diversity

To explore the mechanisms by which CRACD loss accelerates SCLC tumorigenesis, we performed single-cell RNA-sequencing (scRNA-seq) of SCLC tumors isolated from the lung tissues of RPR2 and CRPR2 mice (fig. S3A). Two datasets (RPR2 and CRPR2) were integrated and annotated for each cell type (Fig. 3A, B, S3). Epithelial tumor cell clusters were selected for further unsupervised sub-clustering (Fig. 3B, Table S3). While 13 different cell clusters (clusters 2 and 4-15) were found in RPR2 tumors, 15 types of cell clusters (clusters 1-15) were identified in CRPR2 tumors (Fig. 3C). Overall, clusters 4-15 showed relatively higher expression of NE markers (*Ascl1*, *Calca*, and *Chga*) than clusters 1-3. Clusters 8-10 and 12 were enriched with cell proliferation markers (*Pcna*, *Pclaf*, and *Mki67*) (Fig. 3C). Relative to RPR2 tumors, CRPR2 tumors showed an increased ratio of cell clusters 4, 6, and 7. Conversely, cluster 8 was markedly reduced in CRPR2 tumors. In addition, three cell clusters (1, 3, and 14) were almost exclusively observed in CRPR2 tumors (Fig. 3C, D).

Since *Cracd* KO affects the diversity of cell phenotypes seen in CRPR2 tumors, we explored whether it might affect tumor cell plasticity by inferring cell lineage trajectories using the RNA velocity algorithm (22). The analysis using the scVelo package (22) failed to identify significant differences in cell lineage trajectories between RPR2 and CRPR2 tumors (fig. S4A). However, a computational method that predicts cell fate transitions based on differential geometry using the Dynamo algorithm (23) suggested that CRPR2 tumors exhibited a more complex pattern of cell lineage trajectories than did RPR2 tumors (fig. S4B, Movie S1). Partition-based graph abstraction analysis further supported that CRACD loss increased phenotypic cell diversity (fig. S4C). We next assessed the effect of *Cracd* KO on cell de-differentiation using the CytoTRACE algorithm, which infers cell state (differentiation vs. de-differentiation) (24). Most cell clusters of CRPR2 tumors showed relatively higher cell de-differentiation potential, i.e., less differentiation than did those of RPR2 tumors (Fig. 3E, F). The scRNA-seq analysis from the allograft tumors derived from *Cracd* WT and KO preSCs also predicted that *Cracd* KO altered cell lineage trajectories (fig. S5, S6, Table S4, Movie S1).

To understand how CRACD loss enhances tumor cell diversity, we identified key transcriptional circuits activated in cell clusters of CRPR2. A comparative geneset enrichment assay (GSEA) showed that compared to RPR2, the genesets of distinct cell clusters of CRPR2 were associated with activation of the epithelial-mesenchymal transition, hypoxia, MYC, and E2F pathways (Fig. 3G, H, fig. S7). It is noteworthy that the cell clusters 1 and 2 in CRPR2 tumors were enriched with the SCLC genesets (fig. S7), reiterating the relevance of CRACD inactivation to human SCLC. Recent studies classified SCLC into four major subtypes (*ASCL1*, *NEUROD1*, *POU2F3*, and *YAP1*) (9, 11). Compared to RPR2, *Cracd* KO tumors (CRPR2) were enriched in *Ascl1* and *Calca* expression, resembling the transcriptional signature of the ASCL1-subtype of SCLC (Fig. 3I).

Depletion of CD8+ T cells in *Cracd* KO SCLC tumor

Given that immune cells play crucial roles in tumorigenesis by creating a tumor-favorable environment or killing tumor cells (25, 26), we next examined the impact of CRACD loss on the tumor microenvironment. Using scRNA-seq, we profiled immune cells in RPR2 and CRPR2 tumors that developed in the GEMMs (Fig. 4A-C, fig. S8). CRPR2 tumors harbored strikingly fewer $CD8^+$ T cells (6.86% [170 of 2477 cells]) than did RPR2 tumors (65.06% [3484 of 5355 cells]) while showing a slightly higher ratio of naïve T cells to total cell numbers (26.52% [657 of 2477 cells] versus 20.24% [1084 of 5355 cells]) (Fig. 4C-E), which was also confirmed by immunostaining for $CD8^+$ T cells (Fig. 4F, G). Of note, the number of whole T cells and apoptotic cells remained similar between RPR2 and CRPR2 tumors (fig. S9). In addition, the expression of T cell exhaustion markers (*Pd-1* and *Pd-l1/2*) was not affected by *Cracd* KO in CRPR2 tumors compared to in RPR2 tumors (fig. S10A, B). Moreover, compared to RPR2 tumors, CRPR2 tumors displayed a higher number of monocytes (Fig. 4C, D). Given that myeloid-derived suppressor cells (MDSCs) inhibit T cell activation and proliferation (27, 28), we also examined the impact of CRACD loss on MDSCs. Compared to RPR2, CRPR2 tumors showed an upregulation of MDSC marker gene expression in myeloid cells (Fig. 4H, fig. S10C). Consistent with the results from the autochthonous model, scRNA-seq-based immune profiling of preSC-derived allograft tumors also displayed a decrease in $CD8^+$ T cells and an increase in myeloid cells in *Cracd* KO allograft tumors relative to *Cracd* WT tumors (fig. S11, S12). These results suggest that CRACD loss induces immune landscape remodeling, which is most notable for marked $CD8^+$ T cell loss.

Silencing of the MHC-I pathway in *Cracd* KO SCLC

The altered landscape of immune cells in *Cracd* KO SCLC tumors (Fig. 4) compelled us to determine the underlying mechanism of $CD8^+$ T cell loss. We examined the inferred intercellular communication networks between immune cells and SCLC tumor cells (RPR2 vs. CRPR2) using a CellChat package (29). Overall, CRPR2 tumors showed fewer and weaker cellular interactions among different cell types than RPR2 tumors

(Fig. 5A). In the information flow maps, CRPR2 tumors displayed upregulated putative signaling pathways mainly between tumor cells and B and myeloid cells, compared to RPR2 tumors (Fig. 5B). Notably, the antigen processing and presentation–related pathways were significantly downregulated in CRPR2 tumors relative to in RPR2 tumors mostly between SCLC tumor and $CD8^+$ T cells (Fig. 5B). The information flow predicted by CellChat nominated differentially regulated pathways between RPR2 and CRPR2 tumors (Fig. 5C). According to the absolute values and fold changes of information flow, the most downregulated pathway in CRPR2 was the MHC-I pathway (Fig. 5C, fig. S13). The circle plots validated that the MHC-I pathway was barely detected in CRPR2 tumors but was prevalent in RPR2 tumors (Fig. 5D). Moreover, the GSEA confirmed the marked downregulation of the gene sets associated with the antigen processing and presentation, MHC-I pathway, and T cell receptor signaling (Fig. 5E, fig. S14). Since CRPR2 tumors displayed depleted $CD8^+$ T cells (Fig. 4), it is plausible that the impaired MHC-I pathway fails to activate $CD8^+$ T cells. We examined the expression of the MHC-I pathway–related genes. In line with the CellChat results, i.e., loss of the MHC-I pathway, the genes (*H2-Q1/2/4* and *H2-T3*) encoding the α chain of the mouse MHC-I complex were downregulated in CRPR2 tumors compared to RPR2 tumors (Fig. 5F). These data indicate that *Cracd* KO impairs antigen presentation by silencing the MHC-I pathway.

EZH2-mediated suppression of the MHC-I pathway in CRACD inactivation-associated SCLC

Accumulating evidence suggests that the suppression of antigen processing and presentation is one of the immune evasion mechanisms of cancer cells (30-32). Recent studies showed that the MHC-I pathway is modulated by EZH2 (33-37). Intriguingly, GSEA of differentially expressed genes (DEGs; CRPR2 vs. RPR2) showed the association of the CRPR2 gene signatures with the genesets modulated by EZH2 and the polycomb repressive complex 2 (PRC2) (Fig. 6A). As the catalytic subunit of PRC2, EZH2 induces di- or tri-methylation of histone H3 (H3K27me2/3), repressing

transcriptional activation. Since EZH2 was shown to promote SCLC (38), these data led us to examine the role of EZH2 in suppressing the MHC-I pathway by CRACD loss. Immunofluorescent staining and immunoblot-based quantification showed that compared to RPR2 tumors, CRPR2 tumors exhibited increased H3K27me2/3, histone marks for gene repression while reduced H3K27ac, a histone marker for gene activation (Fig. 6B-D). GSK343, an EZH2 inhibitor, de-repressed the expression of *H2-Q1/2/4* and *H2-T3* in the murine SCLC cell line derived from CRPR2 tumors (Fig. 6E). Similarly, the human SCLC cell line (NCI-H2081) that carries a frame-shift mutation in *CRACD* (Q168Tfs*17) showed upregulation of *HLA-A/B/C* transcription by EZH2 inhibition (Fig. 6F). These results suggest that CRACD loss suppresses the MHC-I pathway via EZH2-mediated epigenetic repression. Next, we tested whether EZH2 inhibition suppresses CRACD-inactivated SCLC tumorigenesis in vivo. Under an EZH2 inhibitor (GSK343) treatment, RPR2 and CRPR2 cells did not show a difference in cell growth in vitro (Fig. 6G). However, compared to RPR2, EZH2 inhibition (GSK343) markedly suppressed CRPR2 tumorigenesis in allograft models (Fig. 6H). Not surprisingly, immunostaining for $CD8^+$ T cells showed increased $CD8^+$ T cells infiltrations in tumor niche (Fig. 6I). Moreover, total T cell number also increased in EZH2 inhibited tumors (Fig. 6J). These results implied that EZH2 inhibition may derepress $CD8^+$ T cells infiltrations induced by CRACD KO in allograft models.

To determine the relevance of the findings in *Cracd KO* SCLC in mice to human disease, we re-analyzed scRNA-seq datasets of SCLC patient tumors. Based on the marked downregulation of *CRACD* in the SC1-type (Fig. 1), we determined whether SC1-type SCLC patient tumors recapitulate the distinct features of CRPR2. The SC1-type tumors expressed relatively lower levels of the genes encoding MHC-I and several of the antigen processing and presentation pathway components (*HLA-A*, *B*, *C*, *E*, *LMP2*/*LMP7*, and *TAP1/2*), EZH2 target genes, and PRC2 target genes compared to the SC2-type tumors (Fig. 6K, L), also confirmed by the GSEA results (Fig. 6M). Additionally, we observed the correlated transcriptional expression between *HLA-A/E* and *CRACD* in SCLC (Fig. 6N). Mechanical pulling force driven by the actin

cytoskeleton is required for NOTCH signaling activation (39, 40). NOTCH signaling antagonizes PRC2-mediated gene repression (41, 42). Indeed, NOTCH signaling module score was relatively lower in the SC1-type where CRACD and the MHC-I pathway were downregulated, compared to SC2 (fig. S15).

We also sought molecular signatures specifying the SC1/2. The SC1-type tumors were enriched with the expression of *AGR2* (anterior gradient 2), *CEACAM6* (carcinoembryonic antigen–related cell adhesion molecule 6), *GPRC5A* (G protein-coupled receptor class C group 5 member A), and *LGALS3* (lectin, galactoside-binding, soluble 3) genes. Exclusively, the SC2-type tumors showed the upregulation of *BAZ1A*, *TMSB15A*, *HTATSF1*, and *KIF1A* (Fig. 6O). Of note, four genes (*AGR2*, *CEACAM6*, *GPCR5A*, and *LGALS3*) mainly expressed in the SC1-type are associated with poor prognosis in several solid cancers (43-46). Together, these results strongly suggest that CRACD inactivation suppresses the MHC-I pathway via EZH2.

Discussion

In this study, we report that genetic ablation of *Cracd* accelerates SCLC tumorigenesis and enhances tumor cell diversity in both allograft and autochthonous models that harbor deletions of *Rb1*, *Trp53*, and *Rbl2* alleles. Moreover, *Cracd* depletion results in a significant reduction of CD8+ T cells within the tumor microenvironment, which is driven by EZH2-mediated inhibition of the MHC-I pathway in tumor cells. Single-cell transcriptomic analysis of human SCLC validates the co-occurrence of CRACD inactivation, MHC-I pathway downregulation, and reduced expression of EZH2/PRC2 target genes. Defining the temporal specificity of a tumor suppressor throughout the course of tumor development is pivotal to understanding SCLC pathogenesis. Using the SCLC GEMM, which provides a window into early- and late-stage tumor development, our study elucidates a tumor suppressive role for CRACD in SCLC progression and immune evasion. These findings provide novel insights into SCLC tumorigenesis and establish a new SCLC mouse model lacking T cell-based immune surveillance.

ICB-based immunotherapy is a promising approach for cancer therapy (47-50). But, it is challenged by primary and acquired therapy resistance (51-53). The determinants of durable therapeutic benefit from ICB in patients with SCLC are not well understood, and identifying these determinants could inform strategies to overcome therapeutic resistance and personalize SCLC therapy. The animal models of *Cracd* KO SCLC and transcriptomic analysis of murine and human tumors suggest that loss of CRACD is associated with inactivation of MHC-I expression in tumor cells. This cell-intrinsic change may render tumor cells evasive to CD8+ cytotoxic T cells and result in the loss of T cells in the tumor microenvironment, also known as "cold tumors" (54).

Single-cell transcriptomic analysis defined an SC1-type of human SCLC characterized by inactive CRACD, EZH2-mediated gene repression, and a suppressed

316 MHC-I pathway, distinct from the SC2-type with active CRACD and a functional MHC-I
317 pathway. Given the MHC-I pathway suppression in the SC1-type, it is likely that SC1-
318 type patients may not exhibit a favorable response to T cell-based ICB (i.e., non-
319 responders). Restoring the MHC-I pathway in such tumors, for example, by EZH2
320 inhibition, may be a strategy to reverse the immune-cold phenotype typical of human
321 SCLC. Targeting other vital epigenetic regulators, notably the lysine demethylase
322 LSD1, has also been shown to restore the MHC-I pathway and sensitize SCLC to ICB
323 (55, 56). Whether MHC-I expression in SC1-type tumors can be restored by LSD1
324 inhibition remains to be determined. This study introduces a new approach to stratify
325 SCLC patients based on CRACD inactivation, defining a potential predictive molecular
326 signature for the effectiveness of T cell-based ICB such as anti-PD-1 and CTLA-4
327 immunotherapies.
328
329 The broad transcriptional impact of CRACD inactivation is intriguing, given the
330 known role of the capping protein in regulating actin dynamics. In transforming
331 intestinal epithelial cells and colon cancer cells, the loss of CRACD results in β-catenin
332 release from the cadherin-catenin-actin complex, which then activates a β-catenin-
333 mediated oncogenic transcription program (12). However, it is unlikely that this
334 CRACD/β-catenin axis explains an enhancement of SCLC tumorigenesis, as we
335 recently demonstrated that the β-catenin pathway is dispensable for SCLC tumor
336 development (57).
337
338 Although the molecular mechanisms by which loss of CRACD influences
339 transcription remain to be determined, one mechanism may relate to its role in
340 regulating the NOTCH signaling. Mechanical pulling force driven by the actin
341 cytoskeleton is necessary for activation of NOTCH signaling through receptor
342 endocytosis, ligand-receptor binding, and NOTCH cleavage (39, 40, 58). Moreover,
343 NOTCH signaling antagonizes EZH2-mediated gene repression (41, 42). Thus, it is
344 plausible that CRACD inactivation inhibits NOTCH signaling, which subsequently
345 induces EZH2-mediated gene silencing of the MHC-I pathway for SCLC's immune

evasion. In line with this, the SC1-type where CRACD is downregulated and T cells are depleted exhibits relatively lower module scores for NOTCH signaling and the MHC-I pathways (Fig. 6I, fig. S15). Moreover, *Cracd* KO SCLC mouse tumors (CRPR2) showed the MHCI-1 pathway downregulation with T cell depletion (Fig. 4, 5). The detailed molecular mechanisms by which CRACD inactivation aberrantly controls the transcription of genes related to oncogenic trajectories and the MHC-I pathway remain to be determined in future studies.

Collectively, our integrative approaches identify CRACD as a tumor suppressor of SCLC and demonstrate that CRACD inactivation in SCLC is correlated with inhibition of the antigen presentation pathway and a marked reduction in T cell infiltration. This study provides novel insight into the mechanisms of SCLC development and immune evasion.

Author Contributions

S.Z., K.-B.K., Y.H., K.-S.P., and J.-I.P. conceived and designed the experiments. S.Z., K.-B.K., Y.H., D.-W.K., B.K., Y.H.B., N.A.K., Y.E.H., G.Z., J.Z., and S.J. performed the experiments. S.Z., K.-B.K., Y.H., J.M.C., C.M.R., K.-S.P., and J.-I.P. analyzed the data. J.M.C. and C.M.R. provided the sequencing files and technical support for scRNA-seq analyses. S.Z., K.-S.P., and J.-I.P. wrote the manuscript.

Acknowledgments

We are grateful to Pierre D. McCrea, Malgorzata Kloc, Rachael Miller, and Adriana Paulucci for their insightful comments and to Ann Sutton (Research Medical Library, MD Anderson) for editing the manuscript. This work was supported by the Cancer Prevention and Research Institute of Texas (RP210028 to G.Z., RP200315 to J.-I.P.), the National Cancer Institute (R35 CA263816 to C.M.R.; U01 CA224293 to K.-S.P.; R01 CA193297 and R03 CA256207 to J.-I.P.), and an Institutional Research Grant (MD Anderson to J.-I.P.). The core facilities at MD Anderson (DNA Sequencing and Genetically Engineered Mouse Facility) were supported by National Cancer Institute Cancer Center Support Grant (P30 CA016672). The Research Histology Core at the University of Virginia was supported by National Cancer Institute Cancer Center Support Grant (P30 CA044579). The core facilities at Baylor College of Medicine (Cytometry & Cell Sorting Core and Single Cell Genomics Core) were supported by CPRIT (RP180672, RP200504) and the National Institutes of Health (CA125123, RR024574).

Materials and methods

Mammalian cell culture

Human embryonic kidney 293T (HEK293T) and NCI-H2081 used in this study were purchased from American Type Culture Collection (ATCC). The murine preSC cells have been previously described (18, 59). HEK293T and preSC cells were maintained in a Dulbecco's Modified Eagle's Medium (DMEM) medium containing 10% fetal bovine serum (Thermo Fisher Scientific) and 1% penicillin and streptomycin (Thermo Fisher Scientific). NCI-H2081 was maintained in DMEM: F-12 medium (5% FBS, 1% penicillin/streptomycin, 0.005 mg/mL Insulin, 0.01mg/mL Transferrin, 30 mmol/L Sodium selenite, 10 mmol/L Hydrocortisone, 10 mmol/L β-estradiol, 2 mM L-glutamine). Cells were cultured at 37°C in a humidified incubator supplied with 5% CO_2 air. Mycoplasma contamination was examined using the MycoAlert mycoplasma detection kit (Lonza). See SI Appendix, Table S1 for reagent information.

CRISPR/Cas9-based gene knockout

CRISPR/Cas9 mediated *Cracd* KO in preSC cells was performed according to Zhang laboratory's protocol (60). Control sgRNA sequence target EGFP: 5'-GGGCG AGGAG CTGTT CACCG-3'; sgRNA sequence target *Cracd*: 5'-ACACA CGGCC ATTTT GGTCA-3'. sgRNA sequence is based on our previous study (12).

Virus production and transduction

HEK293T cells in a 10-cm dish were co-transfected with 5 μg of constructs, 5 μg of plasmid Δ8.2 (Plasmid #8455, Addgene), and 3 μg of plasmid VSVG (Plasmid #8454, Addgene). Cells were incubated at 37°C, and the medium was replaced after 12 h. Virus-containing medium was collected 48 h after transfection and supplemented with 8 μg/mL polybrene to infect target cells in 6-well dishes. After 6 h, the medium was changed. After 48 h, the infected cells were selected with 2 μg/mL puromycin.

qRT-PCR

RNAs were extracted by TRIzol (Invitrogen) and used to synthesize cDNAs using the iScript cDNA synthesis kit (Biorad). qRT-PCR was performed using an Applied Biosystems 7500 Real-Time PCR machine with the primers listed in SI Appendix, Table S4. Target gene expression was normalized to that of mouse *Hprt1* and human *HPRT1*. Comparative $2^{-\Delta\Delta Ct}$ methods were used to quantify qRT-PCR results. See SI Appendix, Table S4 for primers information.

Cell proliferation and viability assays

We counted the number of cells using a hematocytometer (Bio-Rad) on growth days according to the manufacturer's protocol. Cell proliferation was determined by crystal violet staining or Cell Counting Kit-8 (Dojindo Laboratories) according to the manufacturer's protocol. For crystal violet staining, plates were rinsed with Phosphate-buffered saline (PBS), fixed with 4% paraformaldehyde solution for 20 min, and stained

with crystal violet solution (0.1% crystal violet, 10% methanol) for 20 min, followed by rinsing with tap water.

Immunoblotting

Whole-cell lysates of cells were prepared using radioimmunoprecipitation assay (RIPA) buffer with protease inhibitors for 30 min at 4°C, followed by centrifugation (4°C, 13,200 r/min for 15 min). Supernatants were denatured in 5 × Sodium dodecyl-sulfate (SDS) sample buffer (200 mmol/L Tris-HCl [pH 6.8], 40% glycerol, 8% SDS, 200 mmol/L dithiothreitol, and 0.08% bromophenol blue) at 95°C for 5 min, followed by Sodium dodecyl-sulfate polyacrylamide gel electrophoresis (SDS-PAGE). We used 2% non-fat dry milk in Tris-buffered saline and Tween-20 (25 mmol/L Tris-HCl pH 8.0, 125 mmol/L NaCl, and 0.5% Tween-20) for immunoblot blocking and antibody incubation. SuperSignal West Pico and Femto reagents (Thermo Fisher Scientific) were used to detect horseradish peroxidase-conjugated secondary antibodies. Detailed information on the antibodies is shown in SI Appendix, Table S1.

Immunofluorescence microscopy

Cells were fixed for 20 min in 4% paraformaldehyde and permeabilized with 0.1% Triton X-100 (in PBS) for 10 min. After three PBS washes, cells were blocked with 2% bovine serum albumin (BSA) for 30 min at ambient temperature. Cells were then incubated with antibodies diluted in 2% BSA at 4°C overnight. After three PBS washes, the cells were incubated with 1 μg/mL Alexa Fluor 488/647-conjugated secondary antibodies (Invitrogen) by shaking at ambient temperature in the dark for 1 h. Cells were washed three times with PBS in the dark and mounted in Prolong Gold Antifade Reagent (Invitrogen). Immunofluorescent staining was observed and analyzed using confocal or fluorescent microscopes (Zeiss) and ZEN software (Zeiss).

Animals

Immunocompromised (BALB/c athymic nude) mice and C57BL/6 mice were purchased from the Jackson Laboratory (Maine, USA). Compound transgenic mice *Rb1*$^{lox/lox}$ *Trp53*$^{lox/lox}$ *Rbl2*$^{lox/lox}$ (RPR2) mice have been previously described (59). For SCLC tumor induction, the lungs of 10-week-old mice were infected with adenoviral Cre via intratracheal instillation as previously described (59, 61). Multiple cohorts of independent litters were analyzed to control for background effects, and both male and female mice were used. Ad-Cracd-Cre particles were produced in Vector Development Laboratory at Baylor College of Medicine. Mice were euthanized by CO_2 asphyxiation followed by cervical dislocation at the indicated time. Tumors were harvested from euthanized mice, fixed with 10% formalin, embedded in paraffin, and sectioned at 5-μm thickness. The sections were stained with hematoxylin and eosin for histological analysis. All mice were maintained in compliance with the guidelines of the Institutional Animal Care and Use Committee of the University of Texas MD Anderson Cancer Center and the University of Virginia School of Medicine. All animal procedures were performed based on the guidelines of the Association for the Assessment and Accreditation of Laboratory Animal Care and institutional (MD

Anderson and the University of Virginia) approved protocols. This study was compliant with all relevant ethical regulations regarding animal research.

Allograft assay

C57BL/6 mice (4 months old) were purchased from the Institutional Veterinary Medicine and Surgery Facility (MD Anderson Cancer Center). Each mouse (n = 6) was subcutaneously injected with 1×10^6 cells into both flanks. 3 mice were injected with *Cracd* WT cells, the other 3 mice were injected with *Cracd* KO cells. Mice were maintained in the Division of Laboratory Animal Resources facility at MD Anderson. Tumor volume was monitored and calculated by measuring with calipers every 3-4 days (volume = [length × width^2] / 2). Tumor burden was calculated by measuring all tumor lesions within the lung to account for the complete tumor burden. Twenty days after transplantation, mice were euthanized, tumors were photographed, and collected to proceed paraffin-embedding for immunostaining or for single-cell RNA sequencing (scRNA-seq).

Mouse lung tumor and allograft tumor preparation

Prior to processing, mouse SCLC and allograft tumors were decontaminated under the dissecting microscope by removing any normal and connective tissues. Then, tumors were transferred to a dry dish and minced into pieces with blades. The tissue was digested in Leibovitz's medium (Invitrogen) with 2 mg/mL Collagenase Type I (Worthington), 2 mg/mL Elastase (Worthington), and 2 mg/mL DNase I (Worthington) at 37 °C for 45 min. The tissue was triturated with a pipet every 15 min of digestion until homogenous. The digestion was stopped with FBS (Invitrogen) to a final concentration of 20%. The cells were filtered with a 70 μm cell strainer (Falcon) and spun down at 5,000 r/min for 1 min. The cell pellet was resuspended in red blood cell lysing buffer (Sigma) for 3 min, spun down at 5,000 r/min for 1 min, and washed with 1 mL ice-cold Leibovitz's medium with 10% FBS. Cells were resuspended in 1 mL ice-cold Leibovitz's medium with 10% FBS and filtered with a cell strainer (20 μm). Dead cells were removed with Dead Cell Removal Kit (Miltenyi Biotec) according to the manufacturer's instructions. Live cells were collected for 10× Genomics library preparation.

scRNA-seq library prep

Single-cell Gene Expression Library was prepared according to the guideline for the Chromium Single Cell Gene Expression 3v3.1 kit (10× Genomics). Briefly, single cells, reverse transcription (RT) reagents, Gel Beads containing barcoded oligonucleotides, and oil were loaded on a Chromium controller (10× Genomics) to generate single-cell GEMS (Gel Beads-In-Emulsions), where full-length cDNA was synthesized and barcoded for each single cell. Subsequently, the GEMS were broken and cDNAs from each single cell were pooled, followed by cleanup using Dynabeads MyOne Silane Beads and cDNA amplification by PCR. The amplified product was then fragmented to optimal size before end-repair, A-tailing, and adaptor ligation. The final library was generated by amplification. The library was performed at the Single Cell Genomics Core at BCM.

scRNA-seq - raw data processing, clustering, and annotation

The Cell Ranger was used for demultiplexing, barcoded processing, and gene counting. The R package Seurat(62) and Python package Scanpy(63) were used for pre-processing and clustering of scRNA-seq data. UMAP was used for dimensional reduction, and cells were clustered in Seurat or Scanpy. Each cluster was annotated based on marker gene information (see SI Appendix, Table S3, S5, the list of marker genes of each cell cluster). Datasets were pre-processed, normalized separately, and annotated based on their marker gene expression. Scanpy was used for human dataset preprocessing and integration. Each dataset was normalized separately and clustered by the “Leiden” algorithm (64). Scanpy was used to concatenate the *Cracd* WT vs. KO dataset and preSC Cracd WT vs. KO samples. Cells with less than 100 genes expressed and more than 20% mitochondrial reads were removed. Genes expressed in less than 20 cells were removed. Gene expression for each cell was normalized and log-transformed. The percentages of mitochondrial reads were regressed before scaling the data. Dimensionality reduction and Leiden clustering (resolution 0.5 ~ 1) was carried out, and cell lineages were annotated based on algorithmically defined marker gene expression for each cluster (sc.tl.rank_genes_groups, method=‘wilcoxon’). The list of differentially expressed genes (DEGs) in *CRPR2 and preSC Cracd KO* was generated by comparing KO vs. WT (sc.tl.rank_genes_groups, groups=['KO'], reference='WT', method='wilcoxon'). More information about the software and algorithms used in this study is shown in SI Appendix, Table S6.

Cell lineage trajectory analysis

RNA velocity(65) was used to predict the future state of individual cells and cell lineage tracing. Cells were filtered, and dimensional reduction was performed following the default parameters using the scVelo and Scanpy packages. RNA velocity was calculated through dynamical model and negbin model, and cells were clustered using the “Leiden” algorithm. RNA velocity for all datasets was performed with the same parameters (n_neighbors=10, n_pcs=40). Velocity streams were analyzed and plotted by scVelo (dynamical model) (22) and Dynamo (negbin model) (23). Velocity pseudotime analysis was done and plotted with the scVelo package (22) to show the cell state (differentiation vs. de-differentiation) of each cell. PAGA(66) analysis was performed and visualized with scVelo package to predict developmental trajectories and explores the connectivity between different cell clusters.

Proportion difference analysis

Differences in clusters from the two datasets were analyzed and plotted using the pandas package (67). Each cell cluster from the integrated dataset was grouped and cluster differences between the two datasets were compared.

Gene set enrichment analysis (GESA)

GSEA was done using the R package “fgsea” (68) based on the DEG list generated by Scanpy. The enrichment value was calculated and plotted with the fgsea package (permutation number = 2,000).

Cell-cell communication analysis

For ligand-receptor interaction-based cell-cell communication analysis of scRNA-seq datasets the ‘CellChat’ (29) package in R (https://www.r-project.org) was used. The integrated dataset was processed using the Seurat package, then clustered and annotated dataset were analyzed by CellChat with default parameters (p-value threshold = 0.05). Epithelial cells were used as a source group, and immune cells were used as target groups.

Pathway score analysis

Scanpy with the ‘scanpy.tl.score_genes’ function was used for the pathway score analysis (63). The analysis was performed with default parameters and the reference genes from the gene ontology biological process or the Kyoto Encyclopedia of Genes and Genomes database (69, 70). The gene list for the score analysis is shown in SI Appendix, Table S6.

Human scRNA-seq data analysis

The scRNA-seq data set of 19 human SCLC patients samples (Patients information is shown in SI Appendix, Table S1) (10) from Human Tumor Atlas Network (HTAN, https://humantumoratlas.org/) was downloaded and analyzed according to the code provided in the original study. The scRNA-seq data set of the 8 normal human lungs (GSE122960, SI Appendix, Table S2) (17) was extracted from the Gene Expression Omnibus (GEO) database and analyzed with Scanpy and Python. First, to match the gene names of our mouse CRPR2 dataset with those of human datasets, we converted mouse gene names into human gene names using the R package biomaRt, which converted 16,780 genes into human genes. The converted CRPR2 dataset and 27 human datasets were concatenated, normalized, and clustered in Scanpy. Batch effects were corrected using “Harmony” (71) algorithm. Then, the dendrogram and correlation matrix heatmap were plotted with Scanpy. The dendrogram shows the distance of each dataset based on principal component analysis, and the correlation matrix heatmap shows Pearson correlation by a color spectrum.

Copy number variation analysis

To detect the genomic stability of groups SC1 and SC2, we performed copy number variations (CNVs) analysis from the gene expression data using the Python package infercnvpy (https://icbi-lab.github.io/infercnvpy/index.html#). We ran infercnvpy on SC1 and SC2 groups using the Normal group (8 human normal lung datasets) as a reference dataset. The gene ordering file containing the chromosomal start and end position for each gene was generated from the human GRCh38 assembly. Chromosome heatmap and CNV scores in the UMAP were plotted with infercnvpy.

605 **Public sequencing database**
606 All TCGA cancer patients' sequencing data referenced in this study were obtained from
607 the TCGA database at cBioPortal Cancer Genomics (http://www.cbioportal.org).
608 Cancer cell line sequencing data from Cancer Cell Line Encyclopedia (CCLE) were
609 extracted from the cBioPortal Cancer Genomics (http://www.cbioportal.org).
610
611 **Data availability**
612 scRNA-seq data are available via the GEO database (GSE218544; log-in token for
613 reviewers: efsxisoijvwzhuh).
614
615 **Code availability**
616 The code used to reproduce the analyses described in this manuscript can be
617 accessed via GitHub (https://github.com/jaeilparklab/CRACD_SCLC_scRNAseq) and
618 will also be available upon request.
619
620 **Statistical analyses**
621 GraphPad Prism 9.4 (Dogmatics) was used for statistical analyses. The Student's *t*-test
622 was used to compare two samples. P values < 0.05 were considered statistically
623 significant. Error bars indicate the standard deviation (s.d.) otherwise described in
624 Figure legends.
625

References

1. Howlader N, Noone A, Krapcho Me, Miller D, Brest A, Yu M, et al. SEER cancer statistics review, 1975–2016. *National Cancer Institute.* 2019;1.
2. Byers LA, and Rudin CM. Small cell lung cancer: where do we go from here? *Cancer.* 2015;121(5):664-72.
3. Bunn Jr PA, Minna JD, Augustyn A, Gazdar AF, Ouadah Y, Krasnow MA, et al. Small cell lung cancer: can recent advances in biology and molecular biology be translated into improved outcomes? *Journal of Thoracic Oncology.* 2016;11(4):453-74.
4. Gazdar AF, Bunn PA, and Minna JD. Small-cell lung cancer: what we know, what we need to know and the path forward. *Nature Reviews Cancer.* 2017;17(12):725-37.
5. Iams WT, Porter J, and Horn L. Immunotherapeutic approaches for small-cell lung cancer. *Nature Reviews Clinical Oncology.* 2020;17(5):300-12.
6. Pakkala S, and Owonikoko TK. Immune checkpoint inhibitors in small cell lung cancer. *Journal of thoracic disease.* 2018;10(Suppl 3):S460.
7. Ragavan M, and Das M. Systemic Therapy of Extensive Stage Small Cell Lung Cancer in the Era of Immunotherapy. *Curr Treat Options Oncol.* 2020;21(8):64.
8. Gay CM, Stewart CA, Park EM, Diao L, Groves SM, Heeke S, et al. Patterns of transcription factor programs and immune pathway activation define four major subtypes of SCLC with distinct therapeutic vulnerabilities. *Cancer cell.* 2021;39(3):346-60. e7.
9. Rudin CM, Poirier JT, Byers LA, Dive C, Dowlati A, George J, et al. Molecular subtypes of small cell lung cancer: a synthesis of human and mouse model data. *Nature Reviews Cancer.* 2019;19(5):289-97.
10. Chan JM, Quintanal-Villalonga Á, Gao VR, Xie Y, Allaj V, Chaudhary O, et al. Signatures of plasticity, metastasis, and immunosuppression in an atlas of human small cell lung cancer. *Cancer Cell.* 2021;39(11):1479-96. e18.
11. Ireland AS, Micinski AM, Kastner DW, Guo B, Wait SJ, Spainhower KB, et al. MYC drives temporal evolution of small cell lung cancer subtypes by reprogramming neuroendocrine fate. *Cancer cell.* 2020;38(1):60-78. e12.
12. Jung YS, Wang W, Jun S, Zhang J, Srivastava M, Kim MJ, et al. Deregulation of CRAD-controlled cytoskeleton initiates mucinous colorectal cancer via beta-catenin. *Nat Cell Biol.* 2018;20(11):1303-14.
13. Jia D, Augert A, Kim D-W, Eastwood E, Wu N, Ibrahim AH, et al. Crebbp loss drives small cell lung cancer and increases sensitivity to HDAC inhibition. *Cancer discovery.* 2018;8(11):1422-37.
14. Peifer M, Fernández-Cuesta L, Sos ML, George J, Seidel D, Kasper LH, et al. Integrative genome analyses identify key somatic driver mutations of small-cell lung cancer. *Nature genetics.* 2012;44(10):1104-10.
15. Ng SR, Rideout III WM, Akama-Garren EH, Bhutkar A, Mercer KL, Schenkel JM, et al. CRISPR-mediated modeling and functional validation of candidate tumor suppressor genes in small cell lung cancer. *Proceedings of the National Academy of Sciences.* 2020;117(1):513-21.

16. George J, Lim JS, Jang SJ, Cun Y, Ozretić L, Kong G, et al. Comprehensive genomic profiles of small cell lung cancer. *Nature.* 2015;524(7563):47-53.
17. Reyfman PA, Walter JM, Joshi N, Anekalla KR, McQuattie-Pimentel AC, Chiu S, et al. Single-cell transcriptomic analysis of human lung provides insights into the pathobiology of pulmonary fibrosis. *American journal of respiratory and critical care medicine.* 2019;199(12):1517-36.
18. Kim D-W, Wu N, Kim Y-C, Cheng PF, Basom R, Kim D, et al. Genetic requirement for Mycl and efficacy of RNA Pol I inhibition in mouse models of small cell lung cancer. *Gene Dev.* 2016;30(11):1289-99.
19. Kim D-W, Kim K-C, Kim K-B, Dunn CT, and Park K-S. Transcriptional deregulation underlying the pathogenesis of small cell lung cancer. *Translational lung cancer research.* 2018;7(1):4.
20. Schaffer BE, Park K-S, Yiu G, Conklin JF, Lin C, Burkhart DL, et al. Loss of p130 Accelerates Tumor Development in a Mouse Model for Human Small-Cell Lung CarcinomaRb, p53, and p130 Collaboratively Suppress SCLC. *Cancer research.* 2010;70(10):3877-83.
21. Gazdar AF, Savage TK, Johnson JE, Berns A, Sage J, Linnoila RI, et al. The comparative pathology of genetically engineered mouse models for neuroendocrine carcinomas of the lung. *Journal of thoracic oncology.* 2015;10(4):553-64.
22. Bergen V, Lange M, Peidli S, Wolf FA, and Theis FJ. Generalizing RNA velocity to transient cell states through dynamical modeling. *Nature biotechnology.* 2020;38(12):1408-14.
23. Qiu X, Zhang Y, Martin-Rufino JD, Weng C, Hosseinzadeh S, Yang D, et al. Mapping transcriptomic vector fields of single cells. *Cell.* 2022;185(4):690-711.e45.
24. Gulati GS, Sikandar SS, Wesche DJ, Manjunath A, Bharadwaj A, Berger MJ, et al. Single-cell transcriptional diversity is a hallmark of developmental potential. *Science.* 2020;367(6476):405-11.
25. Anderson NM, and Simon MC. The tumor microenvironment. *Curr Biol.* 2020;30(16):R921-R5.
26. Bejarano L, Jordão MJ, and Joyce JA. Therapeutic targeting of the tumor microenvironment. *Cancer discovery.* 2021;11(4):933-59.
27. Nagaraj S, Schrum AG, Cho H-I, Celis E, and Gabrilovich DI. Mechanism of T cell tolerance induced by myeloid-derived suppressor cells. *The Journal of Immunology.* 2010;184(6):3106-16.
28. Srivastava MK, Sinha P, Clements VK, Rodriguez P, and Ostrand-Rosenberg S. Myeloid-derived suppressor cells inhibit T-cell activation by depleting cystine and cysteine. *Cancer research.* 2010;70(1):68-77.
29. Jin S, Guerrero-Juarez CF, Zhang L, Chang I, Ramos R, Kuan C-H, et al. Inference and analysis of cell-cell communication using CellChat. *Nature communications.* 2021;12(1):1-20.
30. Jhunjhunwala S, Hammer C, and Delamarre L. Antigen presentation in cancer: insights into tumour immunogenicity and immune evasion. *Nature Reviews Cancer.* 2021;21(5):298-312.

31. Burr ML, Sparbier CE, Chan KL, Chan Y-C, Kersbergen A, Lam EY, et al. An evolutionarily conserved function of polycomb silences the MHC class I antigen presentation pathway and enables immune evasion in cancer. *Cancer cell.* 2019;36(4):385-401. e8.
32. Thompson JC, Davis C, Deshpande C, Hwang W-T, Jeffries S, Huang A, et al. Gene signature of antigen processing and presentation machinery predicts response to checkpoint blockade in non-small cell lung cancer (NSCLC) and melanoma. *Journal for immunotherapy of cancer.* 2020;8(2).
33. Ennishi D, Takata K, Béguelin W, Duns G, Mottok A, Farinha P, et al. Molecular and Genetic Characterization of MHC Deficiency Identifies EZH2 as Therapeutic Target for Enhancing Immune RecognitionMolecular Profile of MHC Deficiency. *Cancer discovery.* 2019;9(4):546-63.
34. Staehli F, Ludigs K, Heinz LX, Seguín-Estévez Q, Ferrero I, Braun M, et al. NLRC5 deficiency selectively impairs MHC class I-dependent lymphocyte killing by cytotoxic T cells. *The Journal of Immunology.* 2012;188(8):3820-8.
35. Lorenzi S, Forloni M, Cifaldi L, Antonucci C, Citti A, Boldrini R, et al. IRF1 and NF-kB restore MHC class I-restricted tumor antigen processing and presentation to cytotoxic T cells in aggressive neuroblastoma. 2012.
36. Leonhardt RM, Keusekotten K, Bekpen C, and Knittler MR. Critical role for the tapasin-docking site of TAP2 in the functional integrity of the MHC class I-peptide-loading complex. *The Journal of Immunology.* 2005;175(8):5104-14.
37. Bagai R, Valujskikh A, Canaday DH, Bailey E, Lalli PN, Harding CV, et al. Mouse endothelial cells cross-present lymphocyte-derived antigen on class I MHC via a TAP1-and proteasome-dependent pathway. *The Journal of Immunology.* 2005;174(12):7711-5.
38. Hubaux R, Thu KL, Coe BP, MacAulay C, Lam S, and Lam WL. EZH2 promotes E2F-driven SCLC tumorigenesis through modulation of apoptosis and cell-cycle regulation. *Journal of Thoracic Oncology.* 2013;8(8):1102-6.
39. Meloty-Kapella L, Shergill B, Kuon J, Botvinick E, and Weinmaster G. Notch ligand endocytosis generates mechanical pulling force dependent on dynamin, epsins, and actin. *Dev Cell.* 2012;22(6):1299-312.
40. Gordon WR, Zimmerman B, He L, Miles LJ, Huang J, Tiyanont K, et al. Mechanical Allostery: Evidence for a Force Requirement in the Proteolytic Activation of Notch. *Dev Cell.* 2015;33(6):729-36.
41. Ntziachristos P, Tsirigos A, Van Vlierberghe P, Nedjic J, Trimarchi T, Flaherty MS, et al. Genetic inactivation of the polycomb repressive complex 2 in T cell acute lymphoblastic leukemia. *Nat Med.* 2012;18(2):298-301.
42. Seelk S, Adrian-Kalchhauser I, Hargitai B, Hajduskova M, Gutnik S, Tursun B, et al. Increasing Notch signaling antagonizes PRC2-mediated silencing to promote reprograming of germ cells into neurons. *Elife.* 2016;5.
43. Alavi M, Mah V, Maresh EL, Bagryanova L, Horvath S, Chia D, et al. High expression of AGR2 in lung cancer is predictive of poor survival. *BMC cancer.* 2015;15(1):1-9.
44. Jantscheff P, Terracciano L, Lowy A, Glatz-Krieger K, Grunert F, Micheel B, et al. Expression of CEACAM6 in resectable colorectal cancer: a factor of

independent prognostic significance. *Journal of clinical oncology.* 2003;21(19):3638-46.
45. Zhou H, Telonis A, Jing Y, Xia N, Biederman L, Jimbo M, et al. GPRC5A is a potential oncogene in pancreatic ductal adenocarcinoma cells that is upregulated by gemcitabine with help from HuR. *Cell death & disease.* 2016;7(7):e2294-e.
46. Wang H, Song X, Huang Q, Xu T, Yun D, Wang Y, et al. LGALS3 promotes treatment resistance in glioblastoma and is associated with tumor risk and prognosis. *Cancer Epidemiology, Biomarkers & Prevention.* 2019;28(4):760-9.
47. Robert C. A decade of immune-checkpoint inhibitors in cancer therapy. *Nature Communications.* 2020;11(1):1-3.
48. Topalian SL, Taube JM, Anders RA, and Pardoll DM. Mechanism-driven biomarkers to guide immune checkpoint blockade in cancer therapy. *Nature Reviews Cancer.* 2016;16(5):275-87.
49. Akinleye A, and Rasool Z. Immune checkpoint inhibitors of PD-L1 as cancer therapeutics. *Journal of hematology & oncology.* 2019;12(1):1-13.
50. Bagchi S, Yuan R, and Engleman EG. Immune checkpoint inhibitors for the treatment of cancer: clinical impact and mechanisms of response and resistance. *Annual Review of Pathology: Mechanisms of Disease.* 2021;16:223-49.
51. Morad G, Helmink BA, Sharma P, and Wargo JA. Hallmarks of response, resistance, and toxicity to immune checkpoint blockade. *Cell.* 2021;184(21):5309-37.
52. Kok VC. Current understanding of the mechanisms underlying immune evasion from PD-1/PD-L1 immune checkpoint blockade in head and neck cancer. *Frontiers in oncology.* 2020;10:268.
53. Schoenfeld AJ, and Hellmann MD. Acquired resistance to immune checkpoint inhibitors. *Cancer cell.* 2020;37(4):443-55.
54. Duan Q, Zhang H, Zheng J, and Zhang L. Turning cold into hot: firing up the tumor microenvironment. *Trends in cancer.* 2020;6(7):605-18.
55. Nguyen EM, Taniguchi H, Chan JM, Zhan YA, Chen X, Qiu J, et al. Targeting Lysine-Specific Demethylase 1 Rescues Major Histocompatibility Complex Class I Antigen Presentation and Overcomes Programmed Death-Ligand 1 Blockade Resistance in SCLC. *Journal of thoracic oncology: official publication of the International Association for the Study of Lung Cancer.* 2022;17(8):1014-31.
56. Hiatt JB, Sandborg H, Garrison SM, Arnold HU, Liao S-Y, Norton JP, et al. Inhibition of LSD1 with Bomedemstat Sensitizes Small Cell Lung Cancer to Immune Checkpoint Blockade and T-Cell Killing. *Clinical Cancer Research.* 2022;28(20):4551-64.
57. Kim K-B, Kim D-W, Kim Y, Tang J, Kirk N, Gan Y, et al. WNT5A–RHOA Signaling Is a Driver of Tumorigenesis and Represents a Therapeutically Actionable Vulnerability in Small Cell Lung Cancer. *Cancer Research.* 2022;82(22):4219-33.

58. Luca VC, Kim BC, Ge C, Kakuda S, Wu D, Roein-Peikar M, et al. Notch-Jagged complex structure implicates a catch bond in tuning ligand sensitivity. *Science.* 2017;355(6331):1320-4.
59. Kim KB, Kabra A, Kim DW, Xue Y, Huang Y, Hou PC, et al. KIX domain determines a selective tumor-promoting role for EP300 and its vulnerability in small cell lung cancer. *Sci Adv.* 2022;8(7):eabl4618.
60. Ran F, Hsu PD, Wright J, Agarwala V, Scott DA, and Zhang F. Genome engineering using the CRISPR-Cas9 system. *Nature protocols.* 2013;8(11):2281-308.
61. DuPage M, Dooley AL, and Jacks T. Conditional mouse lung cancer models using adenoviral or lentiviral delivery of Cre recombinase. *Nature protocols.* 2009;4(7):1064-72.
62. Hao Y, Hao S, Andersen-Nissen E, Mauck III WM, Zheng S, Butler A, et al. Integrated analysis of multimodal single-cell data. *Cell.* 2021;184(13):3573-87. e29.
63. Wolf FA, Angerer P, and Theis FJ. SCANPY: large-scale single-cell gene expression data analysis. *Genome Biology.* 2018;19(1):15.
64. Traag VA, Waltman L, and Van Eck NJ. From Louvain to Leiden: guaranteeing well-connected communities. *Sci Rep-Uk.* 2019;9(1):1-12.
65. La Manno G, Soldatov R, Zeisel A, Braun E, Hochgerner H, Petukhov V, et al. RNA velocity of single cells. *Nature.* 2018;560(7719):494-8.
66. Wolf FA, Hamey FK, Plass M, Solana J, Dahlin JS, Göttgens B, et al. PAGA: graph abstraction reconciles clustering with trajectory inference through a topology preserving map of single cells. *Genome Biology.* 2019;20(1):59.
67. McKinney W. *Proceedings of the 9th Python in Science Conference*. Austin, TX; 2010:51-6.
68. Korotkevich G, Sukhov V, Budin N, Shpak B, Artyomov MN, and Sergushichev A. Fast gene set enrichment analysis. *BioRxiv.* 2021:060012.
69. Kanehisa M. Toward pathway engineering: a new database of genetic and molecular pathways. *Sci Technol Jap.* 1996;59:34-8.
70. Ashburner M, Ball CA, Blake JA, Botstein D, Butler H, Cherry JM, et al. Gene ontology: tool for the unification of biology. The Gene Ontology Consortium. *Nat Genet.* 2000;25(1):25-9.
71. Korsunsky I, Millard N, Fan J, Slowikowski K, Zhang F, Wei K, et al. Fast, sensitive and accurate integration of single-cell data with Harmony. *Nature methods.* 2019;16(12):1289-96.

Figures legends

Figure 1. CRACD inactivation in SCLC

A, Somatic alterations in *CRACD*, *TP53*, *RB1*, *RBL2*, *CREBBP*, and *EP300* in 249 SCLC patient samples. The diagram was generated using OncoPrinter at www.cbioportal.org/oncoprinter.jsp).

B, Distribution and frequency of *CRACD* mutations found in 102 SCLC cell lines and 249 SCLC patient samples, illustrated along the length of protein. The diagram was generated using the Broad Institute Cancer Cell Line Encyclopedia [CCLE] and cBioPortal databases.

C, Types of *CRACD* mutations found in SCLC patients and cell lines.

D, Levels of *CRACD* transcripts in healthy and SCLC patient samples from the TCGA database; **: $P = 0.002$.

E, UMAPs of SCLC tumor cells from 19 SCLC patient tumor samples (54,633 cells) and 8 normal lung samples (24,041 cells). Each dot represents a single cell, colored by a human sample ID (left) and SCLC vs. normal (right).

F, Correlation matrix plot showing pair-wise correlations among the human normal lung and 19 patient tumor samples. The dendrogram shows the distance of each dataset on the basis of principal component analysis, and the Pearson correlation is displayed with a color spectrum. Groups of patients were categorized by dendrogram and correlation.

G, Sankey plot shows the correlation between group SC1- and SC2-type and RU1108a and clinical information (cancer type and stage).

H, I, A copy number variation analysis of SC1- and SC2-type tumors. Copy number variation plot showing the distribution of genomic alterations (gains and loss) in SC1- and SC2-type tumors compared with healthy human lung samples (H). Copy number variation scores were projected into the UMAP of the scRNA-seq dataset from healthy human lung samples and SC1- and SC2-type samples (I).

J, Dot plot showing NE marker gene expression in 19 SCLC patient samples. ANPY (*ASCL1*, *NEUROD1*, *POU2F3*, and *YAP1*)-based classification was noted at the top. Of note, SC1-type patients belong to the A-type of SCLC.

K, Downregulation of *CRACD* gene expression in SC1-type compared to SC2-type; violin plot showing *CRACD* gene expression between SC1- and SC2-type patient scRNA-seq datasets.

879 **Figure 2. *Cracd* KO accelerates SCLC development in vitro and in vivo**

880 **A-C,** Mouse preSCs were engineered to target *Cracd* alleles using CRISPR-mediated
881 gene editing and characterized for cell morphology (A), short-term proliferation
882 (B), and colony-forming ability (C). Of note, *Cracd*-targeted preSCs readily formed
883 aggregates and spheres typical of SCLC cells.

884 **D,** Representative images of allograft tumors (arrows) derived from preSCs (*Cracd*
885 WT vs. KO) in the flanks of athymic nude mice.

886 **E,** Quantification of tumor development (tumor weight / days taken to reach end-
887 point) in the allograft model.

888 **F-I,** Analysis of autochthonous mouse models: RPR2 (*Rb1, Trp53, Rbl2* triple KO) vs.
889 CRPR2 (*Cracd, Rb1, Trp53, Rbl2* quadruple KO). Representative images of whole
890 lungs (RPR2 vs. CRPR2) (F) and hematoxylin-and-eosin–stained lung sections (G).
891 Tumor burden (H) and proliferative cell quantification (I).

892 **J,** Immunostaining of MKI67 in RPR2 and CRPR2 tumors. Nuclei were counterstained
893 with DAPI. Scale bars = 40 μm.

894 **K,** Quantification of immunostaining results (**J**). Representative images are shown. *P*
895 values were calculated using the Student's *t*-test; error bars: standard deviation
896 (SD).

897

898

899

900 **Figure 3. Increased intratumoral heterogeneity in *Cracd* KO SCLC tumors**

901 **A,** UMAPs of the scRNA-seq datasets of RPR2 and CRPR2 SCLC tumors.

902 **B,** UMAPs of subsets of cells from the global level (left) to SCLC tumor epithelial cells
903 (right). Each dot represents a single cell, colored by cell type. Tumor epithelial
904 cells (RPR2 and CRPR2) were replotted into another UMAP (right).

905 **C,** UMAPs of cell types within RPR2 (left) and CRPR2 cell subsets (right). The top two
906 genes that were highly expressed in each cluster were used for cell cluster
907 annotation of the UMAPs.

908 **D,** Comparison of proportions of different cell types between the RPR2 and CRPR2
909 datasets.

910 **E,** CytoTRACE scores of RPR2 and CRPR2 datasets were analyzed and plotted.

911 **F,** Boxplots of the cell differentiation potential of each cell cluster based on the
912 CytoTRACE score analysis; diff.: cell differentiation; **: $P < 0.01$; ***: $P < 0.001$.

913 **G,** GSEA of gene sets associated with the epithelial-mesenchymal transition pathway
914 and hypoxia pathway in cluster 4 in CRPR2 datasets compared to in RPR2
915 scRNA-seq datasets; NES, normalized enrichment score.

916 **H,** Feature plots displaying the expression of epithelial-mesenchymal transition
917 marker *Vim* and *Fn1*, hypoxia marker *Hif1a*.

918 **I,** Violin (left) and feature (right) plots visualizing *Ascl1* and *Calca* expression between
919 RPR2 and CRPR2 datasets.

920

921

922

Figure 4. Immune landscape remodeling in *Cracd* KO SCLC tumors

A, UMAPs of cells from the global level (left; modified from Figure 3B) and immune cell subsets (right) in RPR2 and CRPR2 scRNA-seq datasets. Each dot represents a single cell, colored by cell type.

B, UMAP of re-clustered whole immune cells of integrated RPR2 and CRPR2 datasets (left). Each cluster represents different immune cell types. Feature plots displaying the expression of T cell marker *Cd3d* and *Cd3g*; B cell marker *Cd79a;* NK cell marker Nkg7; Myeloid cell marker *Lyz2* and *Cd68* (right).

C, UMAPs of RPR2 (left) and CRPR2 subsets (right) show different immune cell types.

D, Comparison of cell proportions of each immune cell type between RPR2 and CRPR2 datasets, color-coded by clusters and cell types.

E, Feature plots of *Cd8a* and *Mki67* expression in immune cells between RPR2 and CRPR2 datasets.

F, G, Analysis of tumor-infiltrated $CD8^+$ T cells. Immunostaining of RPR2 and CRPR2 tumors with anti-CD8 antibody (F). Nuclei were counterstained with DAPI. Quantification of $CD8^+$ T cell counts per 660 μm^2 in RPR2 and CRPR2 tumor tissue (G). Representative images are shown. *P* values were calculated using the Student's *t*-test; error bars: SD.

H, Dot plot showing the expression level of MDSC marker genes (*Itgam*, *Cd14*, *Clec4d/e*, *Il1b*, *Arg2*, *Wfdc17*, and *Cd300ld*) in RPR2 and CRPR2 datasets.

Figure 5. MHC-I pathway downregulation by *Cracd* KO

A, Total cell-cell interactions (left) and interaction strength (right) from RPR2 and CRPR2 tumors were analyzed using the CellChat package.

B, Chord plots showing up-regulated (left) and down-regulated (right) signaling pathways in the CRPR2 scRNA-seq dataset compared to the RPR2 dataset, analyzed using CellChat. The inner bar colors represent the cell clusters that receive signals. The inner bar size is proportional to the signal strength received by the cell clusters. Chords indicate ligand-receptor pairs that mediate the interaction between two cell clusters. The chord size is proportional to the signal strength of the given ligand-receptor pair. Of note, for a CellChat analysis, RPR2 and CRPR2 scRNA-seq datasets were reanalyzed and reannotated with the R package Seurat. Tumor cells were subclustered into nine clusters for CellChat.

C, Overall information flow (upper) and relative information flow (lower) of each signaling pathway in RPR2 and CRPR2 tumors, analyzed using CellChat.

D, Circle plots displaying the inferred network of the MHC-I signaling pathway in RPR2 (left) and CRPR2 tumors (right); the thickness of each line connecting the cell clusters indicates the interaction strength, analyzed using CellChat.

E, GSEA of gene sets associated with the MHC-I pathway in CRPR2 datasets compared to in RPR2 scRNA-seq datasets; NES, normalized enrichment score.

F, Dot plot displaying the expression level of the MHC-I pathway–related genes in the RPR2 and CRPR2 datasets.

Figure 6. EZH2-mediated epigenetic suppression of the MHC-I pathway in CRACD-inactivated SCLC subtype.

A, GSEA of DEGs (from CRPR2 vs. RPR2 scRNA-seq datasets).

B-D, Impact of *Cracd* KO on histone modification of mouse SCLC tumors. Immunostaining of SCLC tumors (RPR2 vs. CRPR2) for H3K27ac, H3K27me2, and K3K27me3 (B). Nuclei were counterstained with DAPI. Histone modifications were quantified by analyzing fluorescence intensity per 660 μm^2 using ZEN software (Zeiss) (C). Scale bars = 40 μm. Immunoblotting shows the impact of *CRACD* KO on H3K27ac, H3K27me2, and H3K27me3 in whole-cell lysates of RPR2 and CRPR2 tumors (D). The representative images are shown. *P* values were calculated using the Student's *t*-test; error bars: SD.

E, F, De-repression of the MHC-I pathway–associated genes by EZH2 inhibition. RT-qPCR analysis of genes related to the mouse MHC-I pathway after 72 hr of treatment of the CRPR2 cell line (derived from mouse SCLC tumors) with 20 μmol/L GSK343, an EZH2 inhibitor (E). RT-qPCR analysis of genes related to the human MHC-I pathway after 72 hr of treatment of a human SCLC cell line (NCI-H2081) with GSK343 (20 μmol/L) (F). Data are expressed as mean ± SD (n = 3 independent assays). Of note, GSK inhibition upregulated the expression of the MHC-I-encoding genes (*H2-Q1/2/4* and *H2-T3* [mouse]; *HLA-A/B/C* [human]).

G, Assessment of in vitro response of RPR2 and CRPR2 cells to GSK343; 72 hr after GSK343 treatment, cell viability was measured using Cell Counting Kit-8 (CCK-8), error bars: SD.

H, Suppression of in vivo tumorigenesis of CRPR2 cells by EZH2 inhibition. Mice subcutaneously injected with CRPR2 cells were treated with vehicle or GSK343 (20 mg/kg, every other day from 5 days after transplantation; intraperitoneal injection). Average tumor volumes at the indicated time points are plotted. error bars: SD.

I, Immunostaining of CRPR2 allograft tumors with anti-CD8 antibody (left), Nuclei were counterstained with DAPI. Quantification of $CD8^+$ T cell counts per 210 μm^2 in CRPR2 tumor tissue (right). Representative images are shown. *P* values were calculated using the Student's *t*-test; error bars: SD.

J, Tumor-infiltrated T cells were stained with CD3, a marker for T cells (left), and T cells were counted per 210 μm^2 in CRPR2 tumor tissues (right). Nuclei were counterstained with DAPI. Representative images are shown. *P* values were calculated using the Student's *t*-test; error bars: SD.

K, Dot plot showing the expression of the MHC-I pathway genes, EZH2 target genes, and PRC2 target genes, in human SCLC tumor samples (SC1- and SC2-type).

L, Violin plot visualizing the expression of the MHC-I pathway–related genes (*HLA-A*, *B*, *C*, *E*, and *TAP1/2*) between SC1- and SC2-type patient datasets.

M, GSEA of gene sets associated with EZH2 targets, PRC2 targets, the MHC-I pathway, and antigen-processing and presentation in SC1- compared to SC2-type tumors.

N, Correlation scatter plot analysis showing the relationship between *CRACD* and MHC-I genes (*HLA-A*, *B*, *C*, *E*, and *TAP1/2*). Pearson's correlation analysis (using GraphPad Prism) showed a positive transcriptional correlation between *CRACD* and MHC-I genes (*HLA-A*, *B*, *C*, *E*, and *TAP1/2*) in SCLC patient tumor cells that express both CRACD and MHC-I genes (*HLA-A*, *B*, *C*, *E*, and *TAP1/2*). r, Pearson correlation coefficient. *P* values were calculated using the Student's *t*-test.

O, Representative marker gene expression of SC1- and SC2-type tumors were visualized for each patient. Genes that were specifically expressed in each group were selected from the differentially expressed gene analysis using the Wilcoxon method.

Figure 1

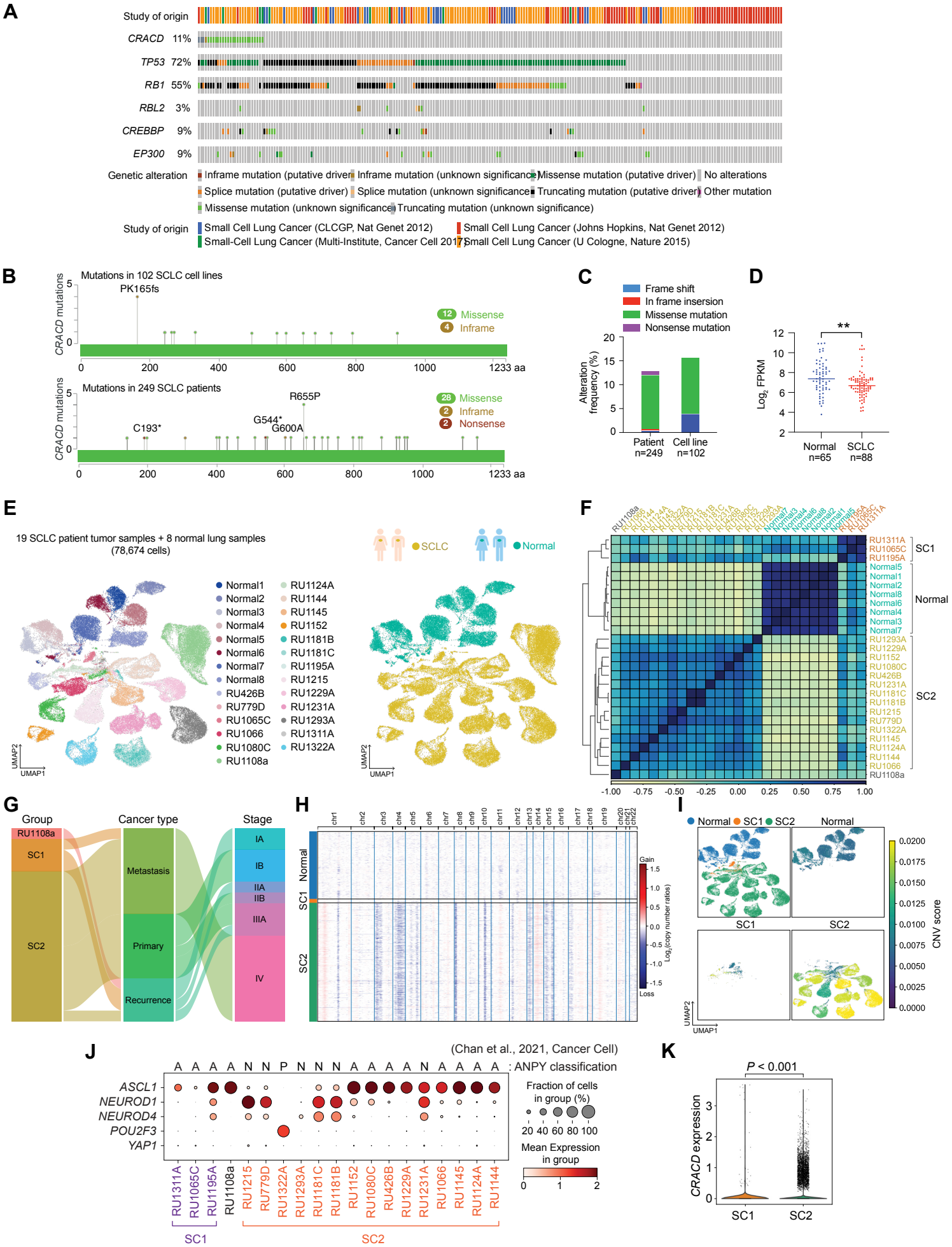
A
Study of origin
CRACD 11%
TP53 72%
RB1 55%
RBL2 3%
CREBBP 9%
EP300 9%
Genetic alteration
Inframe mutation (putative driver)
Inframe mutation (unknown significance)
Missense mutation (putative driver)
No alterations
Splice mutation (putative driver)
Splice mutation (unknown significance)
Truncating mutation (putative driver)
Other mutation
Missense mutation (unknown significance)
Truncating mutation (unknown significance)
Study of origin
Small Cell Lung Cancer (CLCGP, Nat Genet 2012)
Small Cell Lung Cancer (Johns Hopkins, Nat Genet 2012)
Small-Cell Lung Cancer (Multi-Institute, Cancer Cell 2017)
Small Cell Lung Cancer (U Cologne, Nature 2015)
B
Mutations in 102 SLCC cell lines
PK165fs
12 Missense
4 Inframe
Mutations in 249 SLCC patients
R655P
C193*
G544*
G600A
28 Missense
2 Inframe
2 Nonsense
CRACD mutations
1233 aa
C
Frame shift
In frame insersion
Missense mutation
Nonsense mutation
Alteration frequency (%)
Patient n=249
Cell line n=102
D
Log2 FPKM
Normal n=65
SCLC n=88
E
19 SCLC patient tumor samples + 8 normal lung samples
(78,674 cells)
SCLC
Normal
UMAP1
UMAP2
F
SC1
Normal
SC2
G
Group
Cancer type
Stage
RU1108a
SC1
SC2
Metastasis
Primary
Recurrence
IA
IB
IIA
IIB
IIIA
IV
H
Gain
Loss
Log2(copy number ratios)
I
Normal
SC1
SC2
CNV score
J
(Chan et al., 2021, Cancer Cell)
: ANPY classification
ASCL1
NEUROD1
NEUROD4
POU2F3
YAP1
Fraction of cells in group (%)
Mean Expression in group
K
P < 0.001
CRACD expression

Figure 2

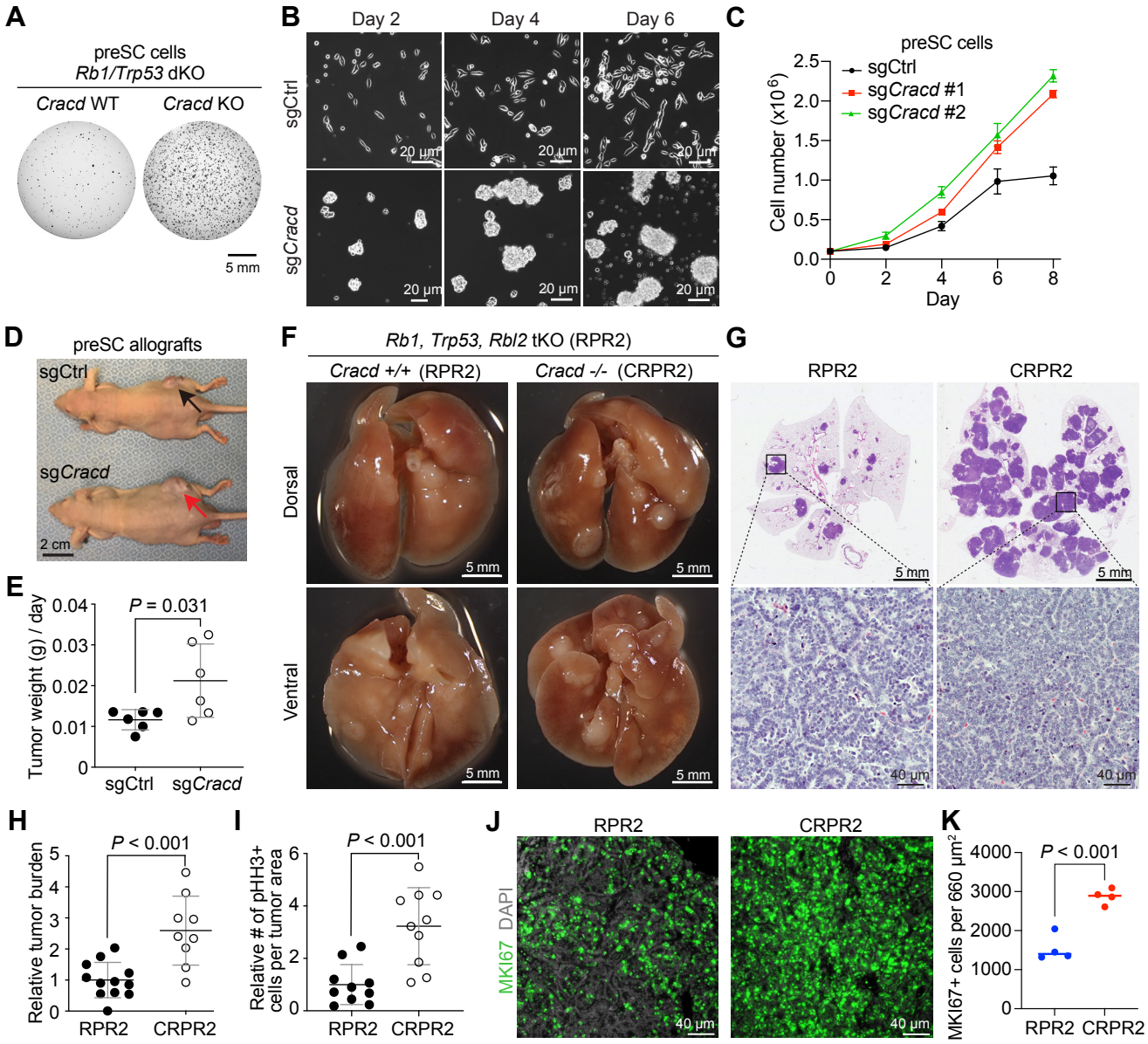
A
preSC cells
Rb1/Trp53 dKO
Cracd WT
Cracd KO
5 mm
B
Day 2
Day 4
Day 6
sgCtrl
sgCracd
20 µm
C
preSC cells
sgCtrl
sgCracd #1
sgCracd #2
Cell number (x10^6)
Day
D
preSC allografts
sgCtrl
sgCracd
2 cm
E
P = 0.031
Tumor weight (g) / day
sgCtrl
sgCracd
F
Rb1, Trp53, Rbl2 tKO (RPR2)
Cracd +/+ (RPR2)
Cracd -/- (CRPR2)
Dorsal
Ventral
5 mm
G
RPR2
CRPR2
40 µm
H
P < 0.001
Relative tumor burden
RPR2
CRPR2
I
P < 0.001
Relative # of pHH3+ cells per tumor area
RPR2
CRPR2
J
RPR2
CRPR2
MKI67 DAPI
40 µm
K
P < 0.001
MKI67+ cells per 660 µm²
RPR2
CRPR2

Figure 3

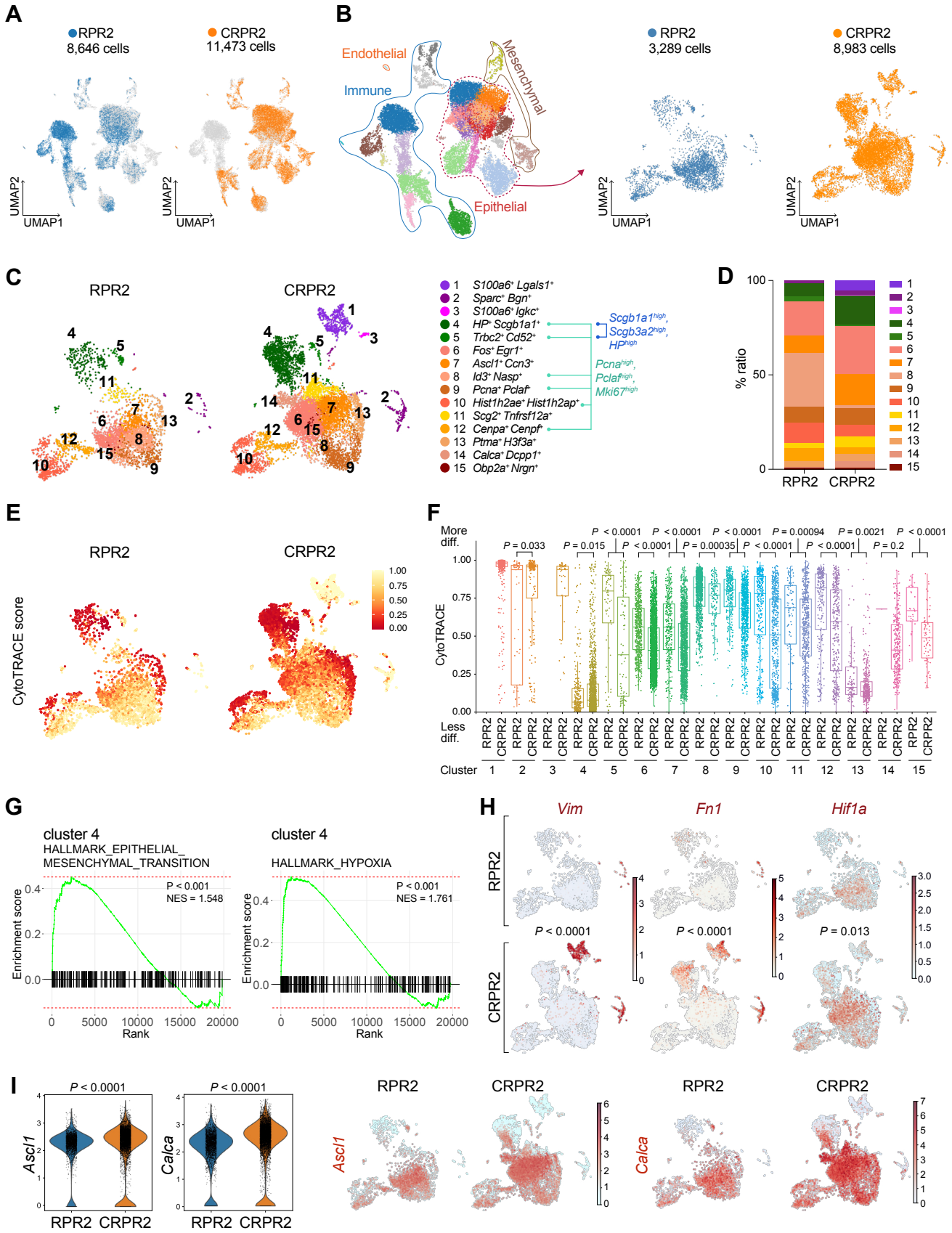
A
RPR2
8,646 cells
CRPR2
11,473 cells
UMAP2
UMAP1
B
Endothelial
Immune
Mesenchymal
Epithelial
RPR2
3,289 cells
CRPR2
8,983 cells
C
RPR2
CRPR2
1 S100a6+ Lgals1+
2 Sparc+ Bgn+
3 S100a6+ Igkc+
4 HP+ Scgb1a1+
5 Trbc2+ Cd52+
6 Fos+ Egr1+
7 Ascl1+ Ccn3+
8 Id3+ Nasp+
9 Pcna+ Pclaf+
10 Hist1h2ae+ Hist1h2ap+
11 Scg2+ Tnfrsf12a+
12 Cenpa+ Cenpf+
13 Ptma+ H3f3a+
14 Calca+ Dcpp1+
15 Obp2a+ Nrgn+
Scgb1a1high, Scgb3a2high, HPhigh
Pcnahigh, Pclafhigh, Mki67high
D
% ratio
100
50
0
RPR2
CRPR2
E
RPR2
CRPR2
CytoTRACE score
1.00
0.75
0.50
0.25
0.00
F
More diff.
Less diff.
CytoTRACE
P = 0.033
P = 0.015
P < 0.0001
P < 0.0001
P < 0.0001
P = 0.00035
P < 0.0001
P = 0.00094
P < 0.0001
P < 0.0001
P = 0.0021
P = 0.2
P < 0.0001
Cluster 1 2 3 4 5 6 7 8 9 10 11 12 13 14 15
G
cluster 4
HALLMARK_EPITHELIAL_MESENCHYMAL_TRANSITION
P < 0.001
NES = 1.548
cluster 4
HALLMARK_HYPOXIA
P < 0.001
NES = 1.761
Enrichment score
Rank
H
Vim
Fn1
Hif1a
RPR2
CRPR2
P < 0.0001
P < 0.0001
P = 0.013
I
P < 0.0001
P < 0.0001
Ascl1
Calca
RPR2
CRPR2

Figure 4

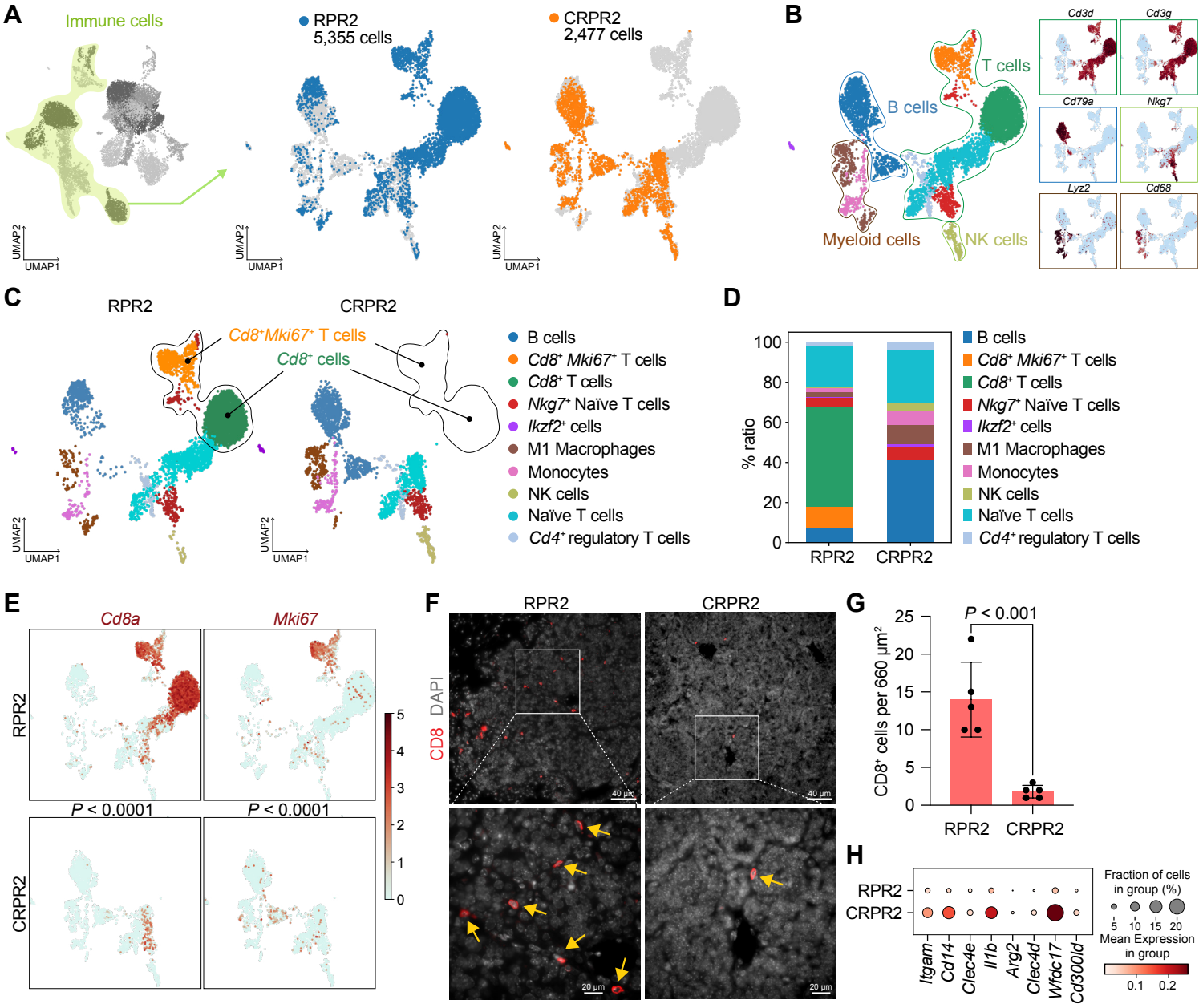
A
Immune cells
RPR2
5,355 cells
CRPR2
2,477 cells
UMAP2
UMAP1
B
T cells
B cells
Myeloid cells
NK cells
Cd3d
Cd3g
Cd79a
Nkg7
Lyz2
Cd68
C
RPR2
CRPR2
Cd8+Mki67+ T cells
Cd8+ cells
B cells
Cd8+ Mki67+ T cells
Cd8+ T cells
Nkg7+ Naïve T cells
Ikzf2+ cells
M1 Macrophages
Monocytes
NK cells
Naïve T cells
Cd4+ regulatory T cells
D
% ratio
100
80
60
40
20
0
RPR2
CRPR2
E
Cd8a
Mki67
RPR2
CRPR2
P < 0.0001
P < 0.0001
5
4
3
2
1
0
F
RPR2
CRPR2
CD8 DAPI
40 µm
20 µm
G
P < 0.001
CD8+ cells per 660 µm2
25
20
15
10
5
0
RPR2
CRPR2
H
RPR2
CRPR2
Itgam
Cd14
Clec4e
Il1b
Arg2
Clec4d
Wfdc17
Cd300ld
Fraction of cells in group (%)
5
10
15
20
Mean Expression in group
0.1
0.2

Figure 5

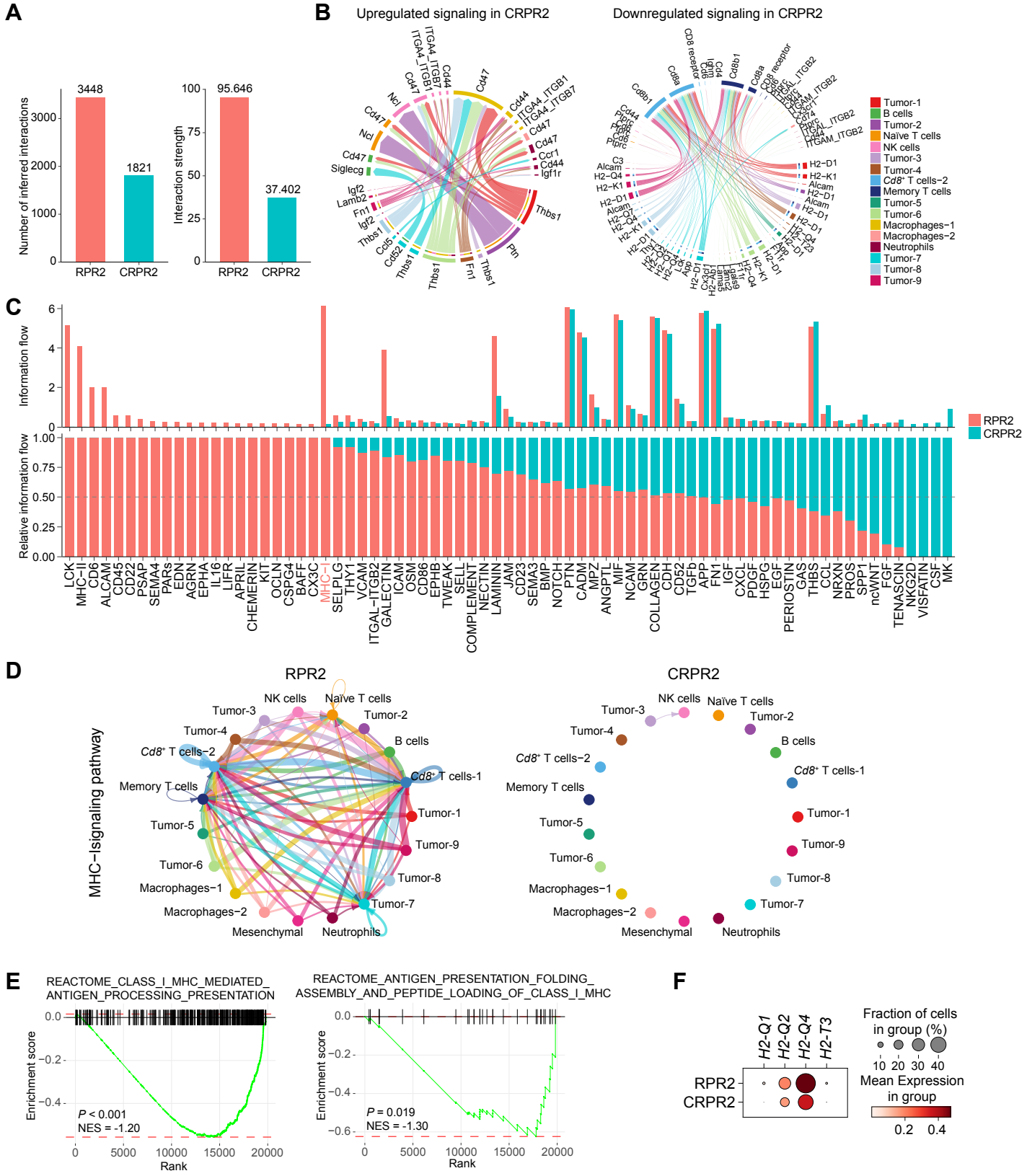
A
Number of inferred interactions
3448
1821
RPR2
CRPR2
Interaction strength
95.646
37.402
B
Upregulated signaling in CRPR2
Downregulated signaling in CRPR2
Tumor-1
B cells
Tumor-2
Naïve T cells
NK cells
Tumor-3
Tumor-4
Cd8+ T cells−2
Memory T cells
Tumor-5
Tumor-6
Macrophages−1
Macrophages−2
Neutrophils
Tumor-7
Tumor-8
Tumor-9
C
Information flow
Relative information flow
RPR2
CRPR2
D
RPR2
CRPR2
MHC−I signaling pathway
Cd8+ T cells-1
Mesenchymal
E
REACTOME_CLASS_I_MHC_MEDIATED_ANTIGEN_PROCESSING_PRESENTATION
REACTOME_ANTIGEN_PRESENTATION_FOLDING_ASSEMBLY_AND_PEPTIDE_LOADING_OF_CLASS_I_MHC
Enrichment score
P < 0.001
NES = -1.20
P = 0.019
NES = -1.30
Rank
F
H2-Q1
H2-Q2
H2-Q4
H2-T3
RPR2
CRPR2
Fraction of cells in group (%)
Mean Expression in group

Figure 6

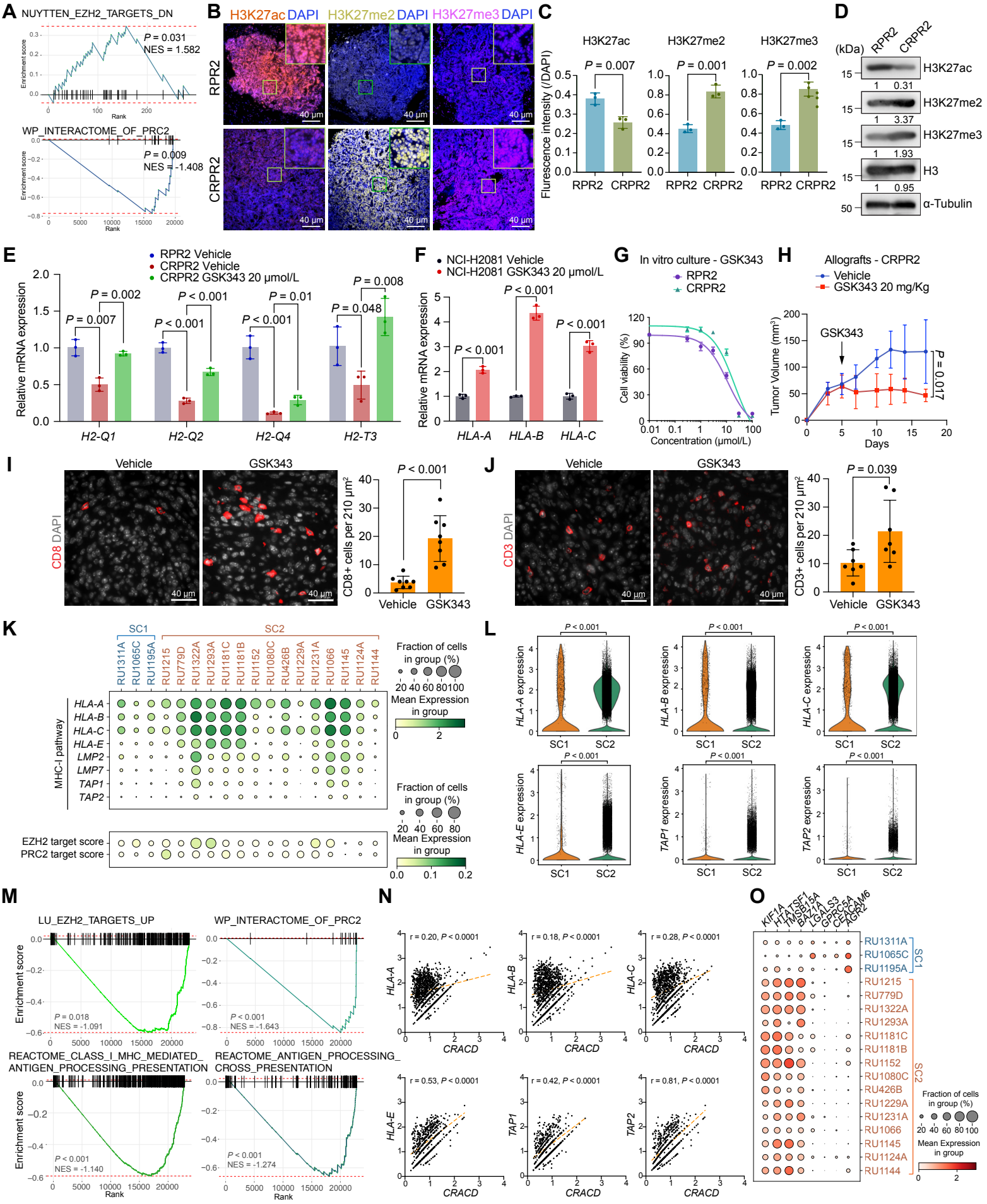
A
NUYTTEN_EZH2_TARGETS_DN
P = 0.031
NES = 1.582
WP_INTERACTOME_OF_PRC2
P = 0.009
NES = -1.408
Enrichment score
Rank
B
H3K27ac DAPI
H3K27me2 DAPI
H3K27me3 DAPI
RPR2
CRPR2
40 μm
C
H3K27ac
H3K27me2
H3K27me3
P = 0.007
P = 0.001
P = 0.002
Flurescence intensity (/DAPI)
RPR2
CRPR2
D
(kDa)
RPR2
CRPR2
H3K27ac
H3K27me2
H3K27me3
H3
α-Tubulin
1 0.31
1 3.37
1 1.93
1 0.95
E
RPR2 Vehicle
CRPR2 Vehicle
CRPR2 GSK343 20 μmol/L
Relative mRNA expression
P = 0.007
P = 0.002
P < 0.001
P < 0.001
P < 0.001
P = 0.01
P = 0.048
P = 0.008
H2-Q1
H2-Q2
H2-Q4
H2-T3
F
NCI-H2081 Vehicle
NCI-H2081 GSK343 20 μmol/L
Relative mRNA expression
P < 0.001
P < 0.001
P < 0.001
HLA-A
HLA-B
HLA-C
G
In vitro culture - GSK343
RPR2
CRPR2
Cell viability (%)
Concentration (μmol/L)
H
Allografts - CRPR2
Vehicle
GSK343 20 mg/Kg
GSK343
Tumor Volume (mm³)
P = 0.017
Days
I
Vehicle
GSK343
CD8 DAPI
40 μm
CD8+ cells per 210 μm²
P < 0.001
Vehicle
GSK343
J
Vehicle
GSK343
CD3 DAPI
40 μm
CD3+ cells per 210 μm²
P = 0.039
Vehicle
GSK343
K
SC1
SC2
RU1311A
RU1065C
RU1195A
RU1215
RU779D
RU1322A
RU1293A
RU1181C
RU1181B
RU1152
RU1080C
RU426B
RU1229A
RU1231A
RU1066
RU1145
RU1124A
RU1144
MHC-I pathway
HLA-A
HLA-B
HLA-C
HLA-E
LMP2
LMP7
TAP1
TAP2
EZH2 target score
PRC2 target score
Fraction of cells in group (%)
20 40 60 80 100
Mean Expression in group
0 2
0.0 0.1 0.2
L
P < 0.001
HLA-A expression
HLA-B expression
HLA-C expression
HLA-E expression
TAP1 expression
TAP2 expression
SC1
SC2
M
LU_EZH2_TARGETS_UP
WP_INTERACTOME_OF_PRC2
P = 0.018
NES = -1.091
P < 0.001
NES = -1.643
REACTOME_CLASS_I_MHC_MEDIATED_ANTIGEN_PROCESSING_PRESENTATION
REACTOME_ANTIGEN_PROCESSING_CROSS_PRESENTATION
P < 0.001
NES = -1.140
P < 0.001
NES = -1.274
Enrichment score
Rank
N
r = 0.20, P < 0.0001
r = 0.18, P < 0.0001
r = 0.28, P < 0.0001
r = 0.53, P < 0.0001
r = 0.42, P < 0.0001
r = 0.81, P < 0.0001
HLA-A
HLA-B
HLA-C
HLA-E
TAP1
TAP2
CRACD
O
KIF1A
HTATSF1
TMSB15A
BAX1A
LGALS3
GPRC5A
CEACAM6
CEACAM5
AGR2
RU1311A
RU1065C
RU1195A
RU1215
RU779D
RU1322A
RU1293A
RU1181C
RU1181B
RU1152
RU1080C
RU426B
RU1229A
RU1231A
RU1066
RU1145
RU1124A
RU1144
SC1
SC2
Fraction of cells in group (%)
20 40 60 80 100
Mean Expression in group
0 2